

# Advanced Weights for IXPE Polarization Analysis

JACK T. DINSMORE<sup>1,2</sup> AND ROGER W. ROMANI<sup>1,2</sup>

<sup>1</sup>*Department of Physics, Stanford University, Stanford CA 94305*

<sup>2</sup>*Kavli Institute for Particle Astrophysics and Cosmology, Stanford University, Stanford CA 94305*

Submitted to ApJ

## ABSTRACT

As the Imaging X-ray Polarimetry Explorer (IXPE) measures increasingly faint sources, the need for precise polarimetry extraction becomes paramount. In addition to previously described neural-net (NN) weights, we introduce here point-spread function weights and particle background weights, which can be critical for faint sources. In some cases these can be augmented by time/phase and energy weights. We provide a publicly available analysis tool to incorporate these new weights, validate our method on simulated data, and test it on archival IXPE observations. Together these weights decrease the area of the polarization uncertainty contour by a factor of two and will be essential for background-limited IXPE observations.

**Keywords:** instrumentation: polarization—methods: data analysis—pulsars: individual (J0534+2200, J0540–6919)—gamma-ray burst: individual (GRB 221009A)

## 1. INTRODUCTION

The Imaging X-ray Polarimetry Explorer (IXPE, Weisskopf et al. 2022; Soffitta et al. 2021) provides unique insights into the geometry of active galactic nuclei, X-ray binaries, pulsar wind nebulae (PWNe) and other X-ray sources. This advance comes from the track images which IXPE’s gas pixel detectors (GPDs, Baldini et al. 2021) provide for each measured X-ray. Much has been achieved with the analytic mission-standard moments (Mom) track analysis which provides estimates of the events’ position, energy, electric vector polarization angle (EVPA), and EVPA accuracy. As we observe fainter IXPE targets exposures become very long and background contamination becomes highly significant; advanced methods to more optimally exploit the track image information become increasingly attractive.

For example Peirson et al. (2021) and Cibrario et al. (2025) introduce neural net (NN)-based methods to extract event parameters from IXPE tracks. Since photon and particle event morphologies differ, Di Marco et al. (2023) suggest cuts based on track metadata that partly suppress particle background. These measurements best constrain source polarization when maximum likelihood estimators (MLE Vianello et al. 2015; Marshall 2021; González-Caniulef et al. 2023; Marshall 2024) are used. Additional refinements are possible.

Prior X-ray observations generally provide detailed image morphology, spectrum, and temporal variation measurements of IXPE targets (e.g. Wong et al. 2023). With accurate IXPE response functions, these measurements allow IXPE event positions, energies, and arrival times to be used as weights, concentrating the statistical power of IXPE data onto the polarization properties.

In this work, we develop a system of track-based weights to improve extraction of source polarization. The NN-technique of (Peirson et al. 2021) already provides effective polarization weights. We introduce a new NN which provides weights for particle rejection. We use new, accurate on-orbit IXPE PSFs (deconvolved from point source observations; Dinsmore & Romani 2024) to provide spatial weights. These weights correct for “polarization leakage” (Bucciantini et al. 2023a), spurious polarized fringes introduced by correlations in errors between the reconstructed event position and EVPA (predicted by Dinsmore & Romani 2024). Section §2 details these weights and their incorporation into an MLE analysis. §3 uses simulations of a polarized point source to show large improvement over the mission-standard extraction, and insensitivity to systematics. We apply the method to published IXPE data in §4, again demonstrating improved uncertainties, and conclude with a brief discussion in §5.

## 2. METHODS

The likelihood  $L$ —the probability distribution function (PDF) of the observed data given the model parameters—may be factored into a product of likelihoods for each event as follows:

$$L = \prod_{\text{event } i} \sum_{\text{source } s} P_s(\psi_i) P_s(\mathbf{r}_i|\psi_i) p_{i,s}. \quad (1)$$

For event  $i$ ,  $P_s(\psi_i)$  and  $P_s(\mathbf{r}_i|\psi_i)$  are the PDFs of EVPA  $\psi_i$  and position  $\mathbf{r}_i$ , assuming an origin from source  $s$ , while  $p_{i,s}$  is the probability that  $i$  was emitted by  $s$ . We use “source” to refer to any potential origin of an IXPE event, which may include astrophysical sources, photon background, or particle background. In Eq. 1,  $P_s(\psi_i)$  and  $P_s(\mathbf{r}_i|\psi_i)$  act as polarization (§2.1) and spatial weights (§2.2).  $p_{i,s}$  may be used to de-weight particle-like events (§2.3) and incorporate spectral and temporal weights (§2.4).

The maximum likelihood estimator (MLE) of parameter  $\theta$  is the value that maximizes  $L$ . With many events, MLE methods are unbiased and deliver optimal uncertainties. Here we estimate the covariance matrix  $\Sigma$  by computing  $(\Sigma^{-1})_{ij} = -\frac{\partial}{\partial\theta_i} \frac{\partial}{\partial\theta_j} \ln L$  at the maximum. The Bayesian approach with wide, uniform priors is equivalent if Gaussian posteriors are assumed, though this assumption may be lifted using a Markov-chain Monte Carlo (MCMC) method. Tools for both types of fits are provided as updates to the `LeakageLib` package, originally designed to treat polarization leakage (Dinsmore & Romani 2024).<sup>3</sup>

### 2.1. Polarization Weights

We define  $q_i = \cos 2\psi_i$  and  $u_i = \sin 2\psi_i$  as the Stokes coefficients of event  $i$ . The PDF of  $\psi_i$  is commonly modeled as

$$P_s(\psi_i) = \frac{1}{2\pi} [1 + \mu_i (Q_s q_i + U_s u_i)], \quad (2)$$

where  $Q_s = \Pi_s \cos 2\Psi_s$  and  $U_s = \Pi_s \sin 2\Psi_s$  are the source’s Stokes coefficients, and  $\Pi_s$  and  $\Psi_s$  are its polarization degree (PD) and angle (PA).

The modulation factor  $\mu_i$  is the PD detected from similar quality events emitted by a 100% polarized source. Such  $\mu_i$  are provided by NN reconstruction (Peirson et al. 2021), using the full event morphology to assess the quality of the polarization measurement. Modulation factors are often approximated by the mean response to events of similar energy  $\mu_i = \mu_{E_i}$ , as measured from simulation or calibration data, but these lack the event quality assessment.

A common analysis technique is to fit a source polarization to all events within an aperture, otherwise disregarding spatial information by considering only this  $P_s(\psi_i)$  term. In the low PD limit of this case, the polarization MLE is analytic:

$$\hat{Q}_{\text{src}} = 2 \frac{\sum_i \mu_i q_i}{\sum_i \mu_i^2}, \quad \hat{U}_{\text{src}} = 2 \frac{\sum_i \mu_i u_i}{\sum_i \mu_i^2}. \quad (3)$$

This result has also been found by Marshall (2021); Bambi & Santangelo (2024) for  $\mu_i = \mu_{E_i}$ , and by the standard Kislat et al. (2015) analysis in the special case of constant  $\mu_{E_i}$ . Full treatment of the additional terms in Eq. 1 offer improvements over these methods.

### 2.2. Spatial Weights

An event arriving from sky coordinate  $\mathbf{x}$  is offset by the point-spread function (PSF) of the telescope and errors in the track reconstruction method. The PDF of the detected position  $\mathbf{r}_i$  is thus

$$P_s(\mathbf{r}_i|\psi_i) \propto \int d^2\mathbf{x} d^2\boldsymbol{\delta} I_s(\mathbf{x}) P_{\text{mir}}(\mathbf{r}_i - \boldsymbol{\delta} - \mathbf{x}) P(\boldsymbol{\delta}|\psi_i) \quad (4)$$

where  $I_s(\mathbf{x})$  is the (generally known) unpolarized surface brightness map of the source,  $P_{\text{mir}}$  is the mirror PSF, and  $\boldsymbol{\delta}$  is the reconstruction error vector. The reconstruction error PDF  $P(\boldsymbol{\delta}|\psi_i)$  depends on the event EVPA, leading to polarization leakage. As in Bucciantini et al. (2023a), we Taylor expand  $P_{\text{mir}}$  in  $\boldsymbol{\delta}$  since  $\boldsymbol{\delta} \ll$  the PSF width. The  $\boldsymbol{\delta}$  integral in Eq. 4 reduces to the first few moments of  $P(\boldsymbol{\delta}|\psi_i)$ , whose values and energy dependence were measured in Dinsmore & Romani (2024). In particular,

$$P_s(\mathbf{r}_i|\psi_i) = C_{i,s}^{-1} \int d^2\mathbf{x} I_s(\mathbf{x}) \left[ I_0(\mathbf{r}_i - \mathbf{x}) + Q_0(\mathbf{r}_i - \mathbf{x}) q_i + U_0(\mathbf{r}_i - \mathbf{x}) u_i + (q_i^2 - u_i^2) X_0(\mathbf{r}_i - \mathbf{x}) + 2q_i u_i Y_0(\mathbf{r}_i - \mathbf{x}) \right] \quad (5)$$

where  $I_0$ ,  $Q_0$ ,  $U_0$ ,  $X_0$ , and  $Y_0$  are the known functions of position and event energy reported in that work, and

$$C_{i,s} = \int d^2\mathbf{r} \int d^2\mathbf{x} I_s(\mathbf{x}) \left[ I_0(\mathbf{r} - \mathbf{x}) + \frac{\mu_i}{2} (Q Q_0(\mathbf{r} - \mathbf{x}) + U U_0(\mathbf{r} - \mathbf{x})) \right] \quad (6)$$

is the normalization constant, obtained by integrating  $P_s(\mathbf{r}_i|\psi_i) P(\psi_i)$  over  $\psi_i$  and  $\mathbf{r}_i$ .

Spatial weights are important for observations of faint sources where they help to de-weight background events. They also correct for polarization leakage biases,

<sup>3</sup> <https://github.com/jtdinsmore/leakagelib>

as we now prove. Consider polarimetry extraction of a bright point source with a small or irregular region, where polarization leakage biases the naive estimator Eq. 3. When spatial weights are included, the likelihood reduces to  $L = \prod_i P(\psi_i) C_{i,s}^{-1}$  (terms that do not depend on the fit parameters are dropped), and the MLE is

$$\begin{aligned}\hat{Q}_{\text{src, spatial}} &= \frac{\sum \mu_i [2q_i - q_0(\mathbf{r}_i)]}{\sum \mu_i^2}, \\ \hat{U}_{\text{src, spatial}} &= \frac{\sum \mu_i [2u_i - u_0(\mathbf{r}_i)]}{\sum \mu_i^2}\end{aligned}\quad (7)$$

where  $q_0(\mathbf{r}) = Q_0(\mathbf{r})/I_0(\mathbf{r})$  and  $u_0(\mathbf{r}) = U_0(\mathbf{r})/I_0(\mathbf{r})$  are the expected leakage patterns. Eq. 7 explicitly demonstrates that our MLE technique correctly subtracts off polarization leakage effects in this simplified limit. We argue that this guarantee extends to more complicated scenarios, provided large data sets and valid source flux models, due to the accuracy of MLE methods.

### 2.3. Background Weights

IXPE data include particle background events, which are often suppressed using cuts outlined in e.g. Di Marco et al. (2023). These cuts are rather weak to minimize loss of true source photons; de-weighting the background can better separate photon and particle signals. We have developed a convolutional neural network (CNN) to provide particle weights. The 28,609 parameter design, built with `tensorflow`, consists of two convolutional layers, max pooling, two more convolutional layers and a dense layer, all with ReLU activation. A final dense layer with sigmoid activation yields a one-dimensional output from 0 to 1 for each event, which we refer to as the “particle character”  $\pi_i$ . Large  $\pi_i$  corresponds to likely particles.

The CNN is trained with binary cross-entropy loss on data sets extracted from IXPE observations of bright, low-polarization point sources (observation IDs 01002401, 01002601, 02002399, and 02001901). The source  $S$  data set consists of events within  $26''$  of the source, while the equal-size background  $B$  data set contains events beyond  $117''$ . We take equal sampling of the 1-10 keV energy range in both data sets so that the trained CNN will not exhibit energy-dependent bias. But the background  $B$  is inevitably polluted by wings of the central PS and astrophysical photon backgrounds. Training on  $B$  and  $S$  gives a initial CNN, used to create a nearly photon-free  $B'$  by removing low  $\pi_i$  (photon) events from  $B$ . We then retrain on  $S$  and  $B'$ . The re-trained CNN performs quite well; 95% of validation events in the  $B'$  (photon-cleaned) data set are cut with a  $\pi_i < 0.5$  threshold. Only 5% of events were misclassified, assuming  $B'$  is perfectly clean. This final CNN and

a script to tag IXPE level 2 files with  $\pi_i$  is provided in the updated version of `LeakageLib`.

Fig. 1 demonstrates the efficacy of particle weights for faint sources using the brightest of all time (B.O.A.T.) Gamma-ray burst as an example. GRB 221009A triggered an IXPE target of opportunity observation (Negro et al. 2023) that began over two days after the burst’s detection and continued for two more. Echos of the initial explosion were detected as faint rings surrounding the point-like afterglow, reflected by Galactic dust. These rings are much more prominent when particles are de-weighted rather than cut, which will be critical for future polarization analyses. Good agreement between the model GRB radial profile (see appendix A) and the IXPE radial profile further illustrates this.

Our CNN assigns high  $\pi_i$  to events cut by Di Marco et al. (2023). Fig. 2 shows our particle character estimates in the space of two level 1 parameters used to determine these cuts. Contours show the event distribution within source ( $r < 10''$ ) and background regions ( $180 < r < 280''$ ) for the IXPE observations of PSR B0540–69. Low  $\pi_i$  events are removed from the background contour to clean it of solar photons. Clearly, the additional information of the NN allows improved background suppression, since some uncut events are flagged with high  $\pi_i$ . De-weighting these events may incur slight source flux loss; our treatment takes this into account when evaluating PD.

The particle character metric  $\pi_i$  output by the CNN is different from the probability that a given event represents a particle  $P_{i,\text{ptcl}}$ ; the latter should take into account the observation’s particle-to-photon flux ratio. By Bayes’ theorem,

$$\frac{\pi_i}{1 - \pi_i} = \frac{F_{\text{ptcl}}}{1 - F_{\text{ptcl}}} \frac{P_{i,\text{ptcl}}}{P_{i,\text{phot}}}\quad (8)$$

where  $F_{\text{ptcl}}$  is the fraction of flux stemming from particles. Note that  $\pi_i = P_{i,\text{ptcl}}$  only for the training data set’s special case of  $F_{\text{ptcl}} = 1/2$ .

In maximum likelihood fits, one assigns all sources  $s$  an emission probability  $p_{i,s} = F_s P_{i,\text{phot}}$  for photon sources and  $p_{i,s} = F_s P_{i,\text{ptcl}}$  for a particle sources, where  $F_s$  is the source flux fraction. Eq. 8 allows  $P_{i,\text{ptcl}}$  to be given in terms of  $P_{i,\text{phot}}$ , which may then be dropped as a constant normalizing factor. The final emission probabilities are

$$p_{i,s} = \begin{cases} F_s & \text{for photon sources} \\ \frac{\pi_i}{1 - \pi_i} F_s & \text{for particle sources} \end{cases}.\quad (9)$$

We fit for  $F_s$  under the  $\sum_s F_s = 1$  constraint.

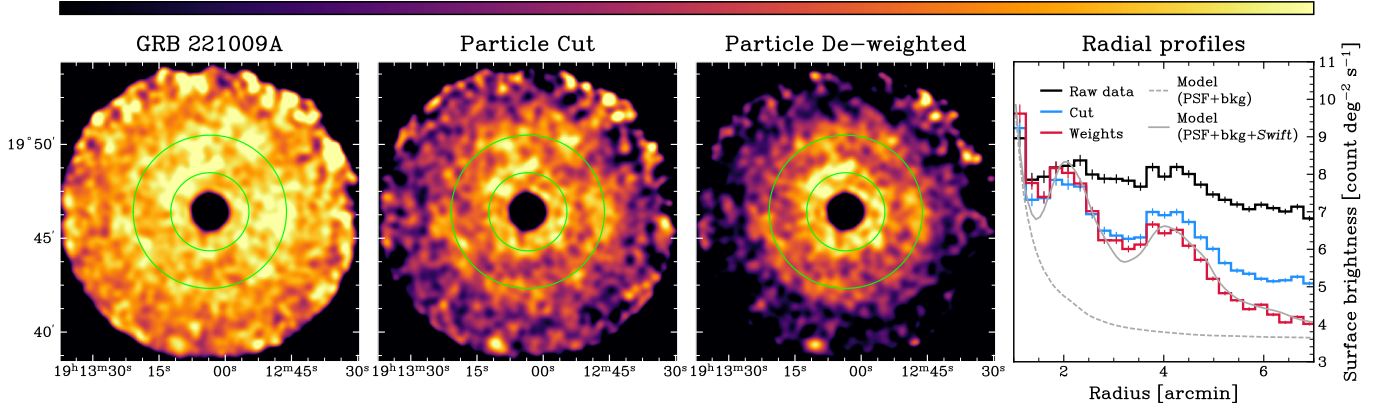


**Figure 1.** The halo representing scattered prompt emission from GRB 221009A with different background removal techniques. *From left:* all 2 – 8 keV counts; counts surviving the background cut of Di Marco et al. (2023); counts weighted by the photon character  $1 - \pi_i$  this work introduces; radial profiles of the images. Green circles highlight the rings as a visual aid. The stretch, max, and min are identical between all panels. The gray curve in the rightmost panel presents a model of the true radial profile derived from the *Swift* GRB 221009A observation, accounting for the IXPE PSF and adding a uniform background.

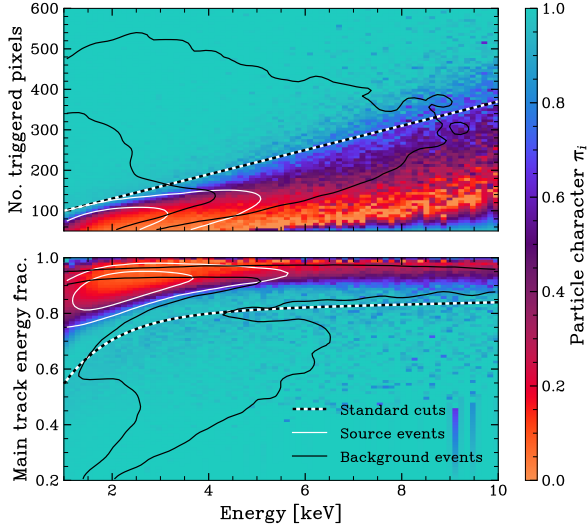


**Figure 2.** The average CNN particle character plotted vs. Mom track properties for PSR B0540-69. The dotted black and white line represents the mission-standard background cuts. 68% and 95% contours of suspected source and background events are also shown. The CNN identifies similar energy dependence of the particle track properties, but enables the use of more precise weighting methods.

#### 2.4. Spectral and Temporal Weights

MLE methods can suffer from bias when applied to observations of multiple bright sources with distinct spectra. In such cases, the events from each source exhibit different modulation factor distributions and the correct distribution must be used to extract polarizations for a given source. For example, consider a polarization MLE for a point source embedded in an unpolarized background. A naive approach would estimate aperture polarization using Eq. 3, measure the counts  $N_{\text{src}}$  ( $N_{\text{bg}}$ ) in source (background) apertures, and multiply the esti-

imator by the background rate  $f_N = N_{\text{src}} / (N_{\text{src}} - \phi N_{\text{bg}})$  where  $\phi$  is the source-to-background area ratio. This method is incorrect because Eq. 3 divides by  $\mu^2$  summed over the entire aperture, which includes both source and spectrum-polluting background events. An unbiased approach is to multiply by a modified background rate

$$f_\mu = \frac{\sum_{i \in \text{src}} \mu_i^2}{\sum_{i \in \text{src}} \mu_i^2 - \phi \sum_{i \in \text{bg}} \mu_i^2}, \quad (10)$$

where  $i \in \text{src}$  and  $i \in \text{bg}$  denote events in the source and background apertures. This normalization accounts for the contaminating background  $\mu$  population.

For more general MLE methods, we account for spectral differences by replacing the flux  $F_s$  in Eq. 9 with a spectrum  $F_s(E_i)$ , multiplying by instrument response functions to account for effective area and energy resolution. The spectral parameters can in principle be simultaneously fit with the polarization to achieve spectropolarimetric fits—potentially useful for detailed spectral studies of brighter sources. But spectral fitting requires modeling of IXPE’s finite energy resolution and is beyond the scope of this work, which focuses on broadband polarimetry of faint sources.

Temporal or phase weights may also be included by replacing  $F_s$  with the lightcurve  $F_s(t_i)$ . Wong et al. (2023) explored this capability in a “simultaneous fitting” analysis of the Crab pulsar and PWN.

### 3. VALIDATION OF SPATIAL AND SPECTRAL WEIGHTING ON SIMULATED DATA

To demonstrate the power of weighted MLE methods, this section compares the Stokes coefficient uncertainties extracted by our analysis and the mission-standard PCUBE algorithm on simulated data. We focus here on



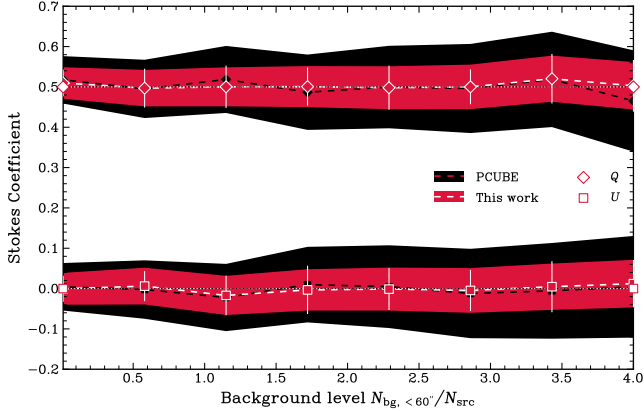


**Figure 3.** Uncertainties as a function of background flux, measured by the ratio of background counts within the 60'' PCUBE radius to source counts. The number of source counts is kept constant. Dotted lines show the true Stokes coefficients, and dashed lines show the coefficients extracted by the two fit methods. Bands reflect the estimated uncertainties. Especially for faint sources, our method delivers substantially more precise fits than PCUBE.

spatial and spectral weights, neglecting particle weights since we lack an accurate simulation of particle events.

PCUBE is a component of the *IXPEobssim* library (Baldini et al. 2022) and reports polarization

$$\hat{Q}_{\text{src}} = 2 \frac{\sum_i (q_i w_i / \mu_i)}{\sum_i w_i}, \quad \hat{U}_{\text{src}} = 2 \frac{\sum_i (u_i w_i / \mu_i)}{\sum_i w_i}, \quad (11)$$

where  $\sum_i$  sums over all  $N$  events in a source aperture, and  $w_i$  is a per-event weight that could be set to the Mom-estimated track weights in a weighted analysis (Di Marco et al. 2022), or unity in an unweighted analysis. This section considers an unweighted analysis. To remove pollution from the unpolarized background, we multiply by  $f_N$  defined in §2.4. Uncertainties on  $\hat{Q}_{\text{src}}$  and  $\hat{U}_{\text{src}}$  are obtained by propagation of errors. Our simulation is of a highly polarized (PD= 50%) point source, with details in appendix B. The simulated background is unpolarized, but we allow the background polarization to vary in our fit when extracting source polarizations as one would when analyzing a real data set.

Fig. 3 shows how background flux affects the accuracy of standard PCUBE (black) and our PSF-weighted analysis (red). Dashed lines and bands give the best-fit values and  $1\sigma$  uncertainties, averaged over many simulated data sets. Both methods produce best-fit Stokes coefficients in agreement with the true values. We also measure the standard deviation of best-fit Stokes coefficients from our method (white error bars). This constitutes a measurement of our method’s uncertainties; Fig. 3 shows they agree with the estimated uncertainty (red band).

For very bright (low background) sources, spatial weighting presents a modest improvement in precision over PCUBE. This improvement is largely due to the bright-source MLE method (Eq. 3), which outperforms the PCUBE approach (Eq. 11). As the background increases, PCUBE uncertainties (and uncertainties from any other aperture-based method) grow, even after background subtraction. However, the spatial weighting strongly suppresses this background so that uncertainties increase very slowly. Thus for faint (especially extended) sources, spatial weighting provides a dramatic improvement.

These simulations are ideal cases, using IXPE’s on-orbit PSFs measured from bright sources. The IXPE aim-point wanders by up to tens of arcseconds over an orbit due to boom drift. In standard processing, this drift is analytically modeled and corrected, but for bright sources we see that the modeling can be imperfect, and we can follow the source motion to remove the residual errors. We measured such residual boom drift patterns for several bright sources and used these to corrupt our simulated data. Even in cases where residual drift reached 17'' (a maximal value), PSF fitting gave Stokes coefficients well within  $1\sigma$  of the true values, and uncertainties were only slightly inflated. In dealing with real data we thus can include a Gaussian ‘blur’ to the spatial model, accounting for residual boom drift, and any small unresolved source extension.

#### 4. APPLICATION TO IXPE DATA

To validate weights performance with real data, we compare the polarization sensitivity of standard analyses with that of our new techniques for three previously analyzed IXPE sources. These are the bright Crab pulsar (PSR B0351+21) and its resolved PWN, the “Crab twin” (PSR B0540–69, hereafter B0540) in the large Magellanic cloud and its unresolved PWN, and GRB 221009A. IXPE observations of these have been well described in earlier publications (Bucciantini et al. 2023b; Xie et al. 2024; Negro et al. 2023, respectively). We report uniform polarizations for the central point source over a broad energy range, although each of these objects also includes more complex spatial, spectral, and temporal polarization behavior. We focus on simple sensitivity here and do not attempt detailed analysis of the signals. In the conclusions we do comment briefly on the methods’ promise for extracting more physics from IXPE data. Descriptions of the analysis for each source are given in appendix D.

The comparison is presented in Fig. 4. Our figure of merit (FoM) is the area of the polarization ellipse  $\sigma_Q \sigma_U$ , with decreased area representing increased sensi-

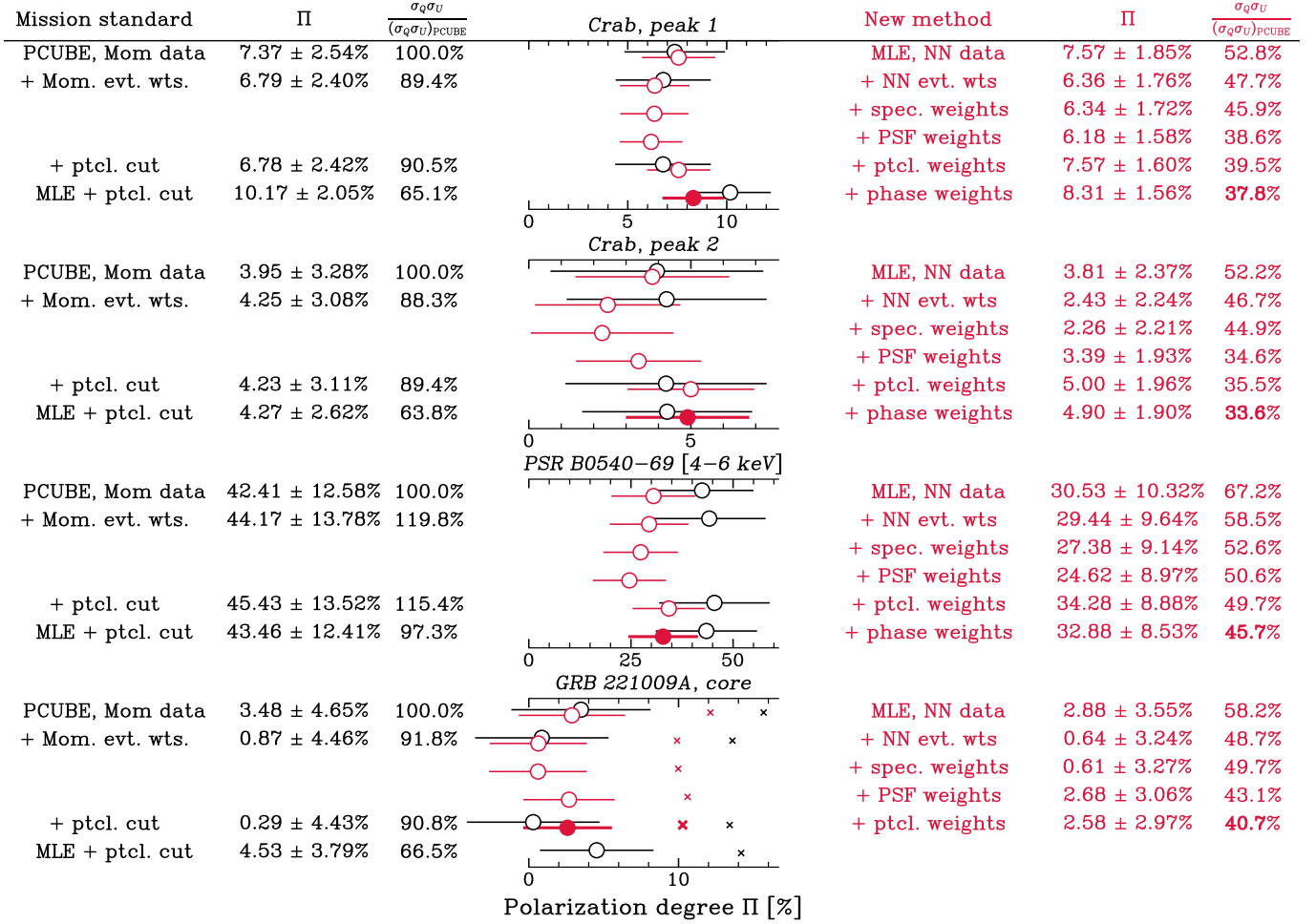


**Figure 4.** Polarization degrees extracted for four point sources using aperture-based methods in common use (*left*) and the weights considered in this work (*right*). Black results use Mom-reconstructed data while red results use NN reconstruction. Uncertainties are expressed in terms of the PD uncertainty and the area of the Q-U uncertainty contour ( $\sigma_Q\sigma_U$ ) relative to the PCUBE area. PD Results are compared in the middle column. The weights introduced in this paper together substantially reduce polarization uncertainties. For the GRB,  $\times$ s indicate 99% confidence upper PD limits since polarization is not detected.

tivity (equivalently, increased effective exposure). It is also important to check that the techniques do not induce undue biases, and so the middle of the figure shows fit PDs and their uncertainty ranges. The left side of the figure shows commonly used aperture-based analysis using Mom reconstruction. On the right we show results from NN reconstructions coupled with new weighting techniques described in this paper.

First on the left, we treat Mom-reconstructed data with unweighted PCUBE (Eq. 11, row 1). Polarization sensitivity generally improves when Mom event weights are added (row 2) and when background is suppressed using the cuts of Di Marco et al. (2023) (row 3). In row 4, we apply the MLE aperture analysis with background rate correction (Eqs. 3 and 10) instead of PCUBE, keeping the particle cut in place but removing Mom event weights. In all cases, this provides better sensitivity than previous rows. We conclude that the MLE-based anal-

ysis using the mean modulation factor is preferred over PCUBE Mom event-weighted analyses. To test whether Mom event weights can improve the MLE analysis, we tried a “weighted MLE analysis” (weighting the sums of Eqs. 3 and 10 with  $w_i$ ). The result improves on the PCUBE weighted analysis, but still possesses larger uncertainties than the unweighted MLE by a factor of 10 – 15%.

On the right, we summarize results from the NN-based weighting techniques. First, NN-reconstruction with the MLE method (Eqs. 3 and 10) and energy-binned modulation factor  $\mu(E_i)$  provides improved sensitivity compared to even the best Mom-bases analysis (row 4, left) and greatly improved sensitivity compared to standard PCUBE (row 1, left). Next, row 2 shows how the sensitivity is further improved by the full event weights  $\mu_i$ . Note that, unlike Mom event weights, these *do* provide an improvement over MLE  $\mu(E_i)$  results, and should be

used. The uncertainties for the above analytical MLE methods are obtained from linear propagation of errors.

Row 3 adds spectral weights, which provide some discrimination between sources.<sup>4</sup> This row and those below are obtained by numerically maximizing the likelihood. Row 4 shows how PSF-weighting improves isolation of the point source from polarized background. This PSF analysis also reduces systematic error from leakage effects which occur for small or non-circular apertures. Small-aperture effects are relevant for Crab, but not quantified here. Next, additional improvement is realized by the NN particle background de-weighting. The effect is very small for these point-source extractions—the improvements should be much more substantial for measurement of faint, extended sources. Finally, to illustrate the effect of additional weights, row 5 shows how phase weighting can improve polarization measurements of the pulsar sources in wide phase windows.

Overall one sees that the weighting improves our sensitivity FoM by  $\gtrsim 2\times$  over simple PCUBE and by  $\gtrsim 30\%$  over even the best current Mom-based analysis. A few special cases deserve comment. While MLE analysis typically offers a large gain, for B0540 we have only measured over 4 – 6 keV to be consistent with the original publication. In this high-energy band, the modulation factor is nearly constant, so the MLE analysis provides little gain over PCUBE. If the detection band can be widened, improvements should be larger. On the other hand, NN reconstruction performs best for these high energy tracks compared to Mom, so NN uncertainties are much reduced. Also, spatial weighting provides good gain when the source/background ratio flux is small. Crab peak 2 is a good example. As noted, background suppression weights offer modest gain for these bright point sources but can be significant for extended faint sources. Our prescription for the background de-weighting appropriately adjusts to the varying circumstances: when background is weak, particle background is only lightly cleaned (e.g. Crab). When particle background is strong, then the weights have a larger effect (e.g. the GRB).

## 5. DISCUSSION AND CONCLUSIONS

This paper highlights the power of NN event analysis and MLE methods to extract polarization measurements from IXPE data. It also introduces new weights which offer additional analysis improvements; detailed instru-

mental PSFs now allow spatial weights and a new NN tool allows improved characterization and de-weighting of likely particle events. Time/phase and energy weighting can also be applied with this formalism. We have validated our method by comparing it analytically to other methods in appropriate limits, recovering true polarizations from simulated data sets, and re-analyzing a varied set of IXPE observations. The results are consistent with, and improve upon, published measurements and show no measurable bias. Compared to the mission standard PCUBE measurement, we reduce the polarization contour area by  $> 2\times$  and make significant improvements to even the best Mom-based polarization analysis. The tools needed to reproduce these results and to apply to other IXPE sources are publicly available in the `LeakageLib` package.

The most effective weighting component depends on source properties. Maximum likelihood estimates are valuable for analyses over wide energy ranges, where the modulation factor varies dramatically. NN track reconstruction always helps, but is most effective when high energy events contribute significantly. Spatial and particle weighting is most useful in the presence of strong backgrounds; spatial weighting has the additional benefit of separating partially resolved sources and removing polarization leakage effects. Phase weighting is important for rapidly varying sources. We caution that these weights are designed for broad band polarization measurements and are not appropriate for spectral analysis. Indeed, bright sources allowing detailed spectral decomposition will not require these weighting techniques and are currently best dealt with other packages, e.g. 3ML or xspec.

This paper applies spatial weights to point sources (albeit with spatially varied backgrounds), but the methods may readily be applied also to extended sources as well. An analysis of a complex field might proceed as follows: an image delivered by the *Chandra* X-ray observatory gives a high-resolution, unpolarized X-ray image, which the astronomer separates into possibly polarized components. The image is rescaled to the IXPE band, and spatially uniform components are added representing solar photons and particles. If necessary for a good fit, these background components should be modeled as polarized. IXPE source polarizations are extracted, using spatial, particle, phase, and/or spectral weights to separate the components. Best results are achieved using NN reconstruction and event weights.

In many cases, IXPE exposures are long and it behooves us to make the best possible use of the collected events. Thus we recommend the use of weighted analysis for all broad-band polarization measurements. Their

<sup>4</sup> Astrophysical spectra are obtained from former studies as reported in appendix D, the solar photon background is assigned a power law with photon index  $\Gamma = 2.5$  which closely matches the data, and NN- and Mom-particle background spectra are measured from data as described in appendix C.

application represents an increase of  $2\times$  or more effective exposure time compared to common unweighted PCUBE measurements. In some cases, e.g. transients such as GRB 221009A, additional data can never be collected in any case, and weighted analysis can enable additional science. For example, with no significant PD bias, the lowered bounds on afterglow polarization (crosses in Figure 4) can be used to exclude otherwise acceptable models. Indeed the X-ray PD bounds are now similar to the optical upper limits reported in [Negro et al. \(2023\)](#). As IXPE attempts to measure ever fainter sources, we expect that the PSF and background weights described here should become increasingly essential.

## APPENDIX

### A. GRB 221009A RADIAL PROFILE MODEL

The Neil Gehrels *Swift* observatory measured GRB 221009A’s expanding rings of prompt emission throughout IXPE’s observation, as [Williams et al. \(2023\)](#) reports. The ring reflected by a certain dust cloud expands such that its angular size in radians is  $\sqrt{2c\Delta t/D}$ , where  $c$  is the speed of light,  $\Delta t$  is the time since the burst, and  $D$  is the distance to the dust cloud (Eq. 1 of [Williams et al. 2023](#)). Its intensity is proportional to the Galactic dust density, reduced by photoelectric absorption for rings reflected by more distant dust (Eq. E1 of [Williams et al. 2023](#)). This allowed the determination of a line-of-sight dust density profile from *Swift* data. We use this density distribution to predict the IXPE radial intensity profile, integrating the result over IXPE’s observing window.

### B. POLARIZATION LEAKAGE FORWARD MODEL

To validate our spatial weights on simulated data in §3, we construct a simulation capable of modeling the relevant effects, including the telescope response functions, PSF, and polarization leakage. While we cannot use the IXPEobssim simulator because it does not model polarization leakage, we otherwise mirror its approach. We draw event energies from power-law spectra with photon indices of 1.5 for the source and 2 for the background. The source spectrum is multiplied by the IXPE effective area and quantum efficiency as given in IXPEobssim. The EVPA  $\psi$  of each event is drawn from the standard Eq. 2. The modulation factor  $\mu$  is also given as a function of energy in IXPEobssim.

Spatially, background events are distributed uniformly and point source events are initially distributed by the mirror PSFs for each IXPE detector. We use the sky-

## ACKNOWLEDGMENTS

This work was supported in part by by contract NNM17AA26C from the MSFC to Stanford in support of the IXPE project. The authors also thank Niccolò Di Lalla, Luca Baldini, and the rest of the IXPE Collaboration for helpful conversations.

*Facilities:* IXPE, CXO

*Software:* LeakageLib ([Dinsmore & Romani 2024](#)), IXPEobssim ([Baldini et al. 2022](#)), HEAsoft ([Nasa High Energy Astrophysics Science Archive Research Center \(Heasarc\) 2014](#))

calibrated PSFs, not the circularly symmetric approximations. The event positions are then offset by a reconstruction error  $\delta$  linked to the event EVPA. To determine  $\delta$ , we use the second moments  $\sigma_{\parallel,\perp}^2(E)$  and the fourth moment parallel component  $k_{\parallel}^4(E)$  of the PDF of  $\delta$  as determined from on-sky data in [Dinsmore & Romani \(2024\)](#). Assuming that all the other moments are Gaussian determines a unique closed functional form for  $P(\mathbf{r}_i|\psi_i)$ : a Gaussian times a series of Hermite polynomials. Values of  $\delta$  are drawn from this distribution.

### C. NEURAL NET EVENT RECONSTRUCTION

The NN developed and trained in [Peirson et al. \(2021\)](#) accurately determines the PA, position, and energy of IXPE events based on the “level 1” raw track files available in the HEASARC data archive. After processing tracks with the `ixpeevtorecon` software, we determine NN track properties and run the results through the standard level 1 to level 2 pipeline, shipped through HEAsoft version 6.35.2. Among other effects, this pipeline corrects for telescope gain, boom drift, and spurious modulation. In particular, the spurious modulation effect—a detector artifact yielding spatially dependent anomalous polarization—will differ between Mom and NN reconstructions. Here we use the modulation amplitude scaling in [Peirson et al. \(2021\)](#) estimated from basic calibration measurements. A more complete analysis of polarized calibration sources in [Cibrario et al. \(2025\)](#) gives similar results.

While the typical difference between NN- and Mom-estimated energies for photon-like tracks is well under 1 keV, on particle-like tracks the methods assign very different energies. From B0540 events with  $\pi_i > 0.5$  at distances of 180–280'' from the source, we measure that



the Mom particle spectrum is approximately a  $\Gamma = 1.87$  power-law, unmodified by the effective area. The NN particle spectrum is harder and non-power-law. These measured spectra are used for the spectral weighted fits reported in the main text.

#### D. DETAILED ANALYSIS METHODOLOGY

This section describes the data reduction and analysis methods used to extract the polarization degrees listed in Fig. 4.

*Crab*—The Crab is bright enough that a single observation (ID 02001601) supplies plenty of signal. We apply the NN-reconstruction method as described in appendix C and phase the data after barycentric correction using the CRABTIME ephemeris database. After aligning the detectors to center the pulsar, our polarization is extracted from a  $25''$  aperture during both the “on” and “off” phases and subtracted to reveal the pulsar polarization. For the spatially weighted methods, we model the nebula within this aperture with a flux map taken from a contemporaneous *Chandra* observation (observation ID 23539), reprocessed, cut to  $2 - 8$  keV, and mapped to the IXPE effective area. Our pulsar spectral model is taken from (Weisskopf et al. 2004) and the nebula spectrum is assumed to exhibit  $\Gamma = 1.9$ , consistent with torus spectra measured in (Mori et al. 2004). Since the polarization maps reported in (Wong et al. 2023) found little PA variation within our region, assuming uniform polarization for this structure is acceptable. Spatial variation of the nebular background will produce unphysical polarization leakage signals that will not average to zero inside the aperture. While the PSF-weighted analysis automatically corrects for this leakage, it is not corrected in the aperture extraction methods.

Our measured background (nebula) PA agrees with that previously determined for the center of the Crab (Wong et al. 2023). For the pulsar, we extract separate PDs for the first (phase  $0.17 - 0.24$ ) and second ( $0.565 - 0.65$ ) peaks. Note that more detailed phase analysis show rapid PA sweeps (Bucciantini et al. 2023a; Wong et al. 2023), so phases values are sensitive to the precise boundaries. However our results in these broad peak bins are consistent with previous measurements and more importantly use identical events for each analysis, allowing useful FoM comparisons.

*PSR B0540–69*—Our B0540 analysis considers IXPE 4–6 keV events from observations 02001201, 02001202, and 02008801, as the original analysis finds significant polarization only in this bin (Xie et al. 2024). When we reprocess NN events, we retain the Mom energy estimates to ensure that we fit to the same events regard-

less of the reconstruction method.<sup>5</sup> We use the same ephemeris, spectrum, and on-off phase bins as that analysis. Our aperture-based methods are conducted with a radius of  $60''$ , and the off-phase is taken as background for the on-phase, similarly to Crab. The PSF-weighted analyses use a  $278''$ -radius aperture, nearly to the chip edge. Using a large aperture is beneficial because the PSF wings provide some useful counts at these large separations, and spatial weighting ensures the extra background events do not harm the fit precision. Our phase-weighted analysis uses the entire available B0540 data set. We see a slight, non-significant drop in PD which would be expected if the PA sweeps over the pulsar period.

The B0540 observation is extended compared to the PSF models. We blur the PSF with a Gaussian, finding a standard deviation of  $8.8''$  from a fit to the merged IXPE image. The extension is likely due to imperfect boom correction, with possible contribution from the  $\sim 5''$ -radius PWN. We treat both the PWN and pulsed emission as point sources under the blurred PSF model, and add faint uniform photon and particle backgrounds. Since a fit shows the backgrounds as consistent with unpolarized to  $1\sigma$ , we assume an unpolarized background in the final analysis.

*GRB 221009A*—Observation 02250101 of the B.O.A.T. was first analyzed using a  $26''$  aperture surrounding the point source (Negro et al. 2023). We use the same radius for aperture-based methods, and assign spectral weights using the spectrum found in that work. Lacking a clean background region, we approximate background flux using a  $160 - 200''$ -radius annulus, which will be slightly polluted by flux from the scattered rings (see Fig. 1). We do not require a clean background region for spatially weighted methods, so for these we remove the background annulus and extend the source aperture to  $60''$ . In principle, this source aperture extension risks including some flux from the extended rings of scattered X-rays from the initial explosion. However, at the time of the IXPE observation, the dust responsible for ring emission within our aperture is at distances  $> 48$  kpc from Earth, where densities are likely quite low (see appendix A). Indeed, a fit that includes a ring component shows that its flux within our aperture is consistent with zero. We therefore ignore the rings in the final spatial weighted fit. We also fit uniform background photon and particle components. As with B0540, we see no

<sup>5</sup> This 2 keV range is not much larger than the IXPE energy resolution, so different event reconstruction can significantly alter the included set.

signal of background polarization and therefore assume that they are unpolarized.

## REFERENCES

- Baldini, L., Barbanera, M., Bellazzini, R., et al. 2021, *Astroparticle Physics*, 133, 102628, doi: [10.1016/j.astropartphys.2021.102628](https://doi.org/10.1016/j.astropartphys.2021.102628)
- Baldini, L., Bucciantini, N., Lalla, N. D., et al. 2022, *SoftwareX*, 19, 101194, doi: <https://doi.org/10.1016/j.softx.2022.101194>
- Bambi, C., & Santangelo, A., eds. 2024, *Handbook of X-ray and Gamma-ray Astrophysics* (Springer), doi: [10.1007/978-981-16-4544-0](https://doi.org/10.1007/978-981-16-4544-0)
- Bucciantini, N., Di Lalla, N., Romani, R. W. R., et al. 2023a, *A&A*, 672, A66, doi: [10.1051/0004-6361/202245744](https://doi.org/10.1051/0004-6361/202245744)
- Bucciantini, N., Ferrazzoli, R., Bachetti, M., et al. 2023b, *Nature Astronomy*, 7, 602, doi: [10.1038/s41550-023-01936-8](https://doi.org/10.1038/s41550-023-01936-8)
- Cibrario, N., Negro, M., Bonino, R., et al. 2025, *ApJ*, 984, 171, doi: [10.3847/1538-4357/ad92c](https://doi.org/10.3847/1538-4357/ad92c)
- Di Marco, A., Costa, E., Muleri, F., et al. 2022, *AJ*, 163, 170, doi: [10.3847/1538-3881/ac51c9](https://doi.org/10.3847/1538-3881/ac51c9)
- Di Marco, A., Soffitta, P., Costa, E., et al. 2023, *AJ*, 165, 143, doi: [10.3847/1538-3881/acba0f](https://doi.org/10.3847/1538-3881/acba0f)
- Dinsmore, J., & Romani, R. 2024, *jtdinsmore/leakagelib*: Publication, v1.0.0, Zenodo, doi: [10.5281/zenodo.10483298](https://doi.org/10.5281/zenodo.10483298)
- Dinsmore, J. T., & Romani, R. W. 2024, *ApJ*, 962, 183, doi: [10.3847/1538-4357/ad2065](https://doi.org/10.3847/1538-4357/ad2065)
- González-Caniulef, D., Caiazzo, I., & Heyl, J. 2023, *MNRAS*, 519, 5902, doi: [10.1093/mnras/stad033](https://doi.org/10.1093/mnras/stad033)
- Kislat, F., Clark, B., Beilicke, M., & Krawczynski, H. 2015, *Astroparticle Physics*, 68, 45
- Marshall, H. L. 2021, *ApJ*, 907, 82, doi: [10.3847/1538-4357/abcf3](https://doi.org/10.3847/1538-4357/abcf3)
- . 2024, *ApJ*, 964, 88, doi: [10.3847/1538-4357/ad0897](https://doi.org/10.3847/1538-4357/ad0897)
- Mori, K., Burrows, D. N., Hester, J. J., et al. 2004, *ApJ*, 609, 186, doi: [10.1086/421011](https://doi.org/10.1086/421011)
- Nasa High Energy Astrophysics Science Archive Research Center (Heasarc). 2014, *HEASoft: Unified Release of FTOOLS and XANADU*, Astrophysics Source Code Library, record ascl:1408.004. <http://ascl.net/1408.004>
- Negro, M., Di Lalla, N., Omodei, N., et al. 2023, *ApJL*, 946, L21, doi: [10.3847/2041-8213/acba17](https://doi.org/10.3847/2041-8213/acba17)
- Peirson, A., Romani, R., Marshall, H., Steiner, J., & Baldini, L. 2021, *Nuclear Instruments and Methods in Physics Research Section A: Accelerators, Spectrometers, Detectors and Associated Equipment*, 986, 164740, doi: <https://doi.org/10.1016/j.nima.2020.164740>
- Soffitta, P., Baldini, L., Bellazzini, R., et al. 2021, *AJ*, 162, 208, doi: [10.3847/1538-3881/ac19b0](https://doi.org/10.3847/1538-3881/ac19b0)
- Vianello, G., Lauer, R. J., Younk, P., et al. 2015, *arXiv e-prints*, arXiv:1507.08343, doi: [10.48550/arXiv.1507.08343](https://doi.org/10.48550/arXiv.1507.08343)
- Weisskopf, M. C., O’Dell, S. L., Paerels, F., et al. 2004, *ApJ*, 601, 1050, doi: [10.1086/380600](https://doi.org/10.1086/380600)
- Weisskopf, M. C., Soffitta, P., Baldini, L., et al. 2022, *Journal of Astronomical Telescopes, Instruments, and Systems*, 8, 026002, doi: [10.1117/1.JATIS.8.2.026002](https://doi.org/10.1117/1.JATIS.8.2.026002)
- Williams, M. A., Kennea, J. A., Dichiara, S., et al. 2023, *ApJL*, 946, L24, doi: [10.3847/2041-8213/acbcd1](https://doi.org/10.3847/2041-8213/acbcd1)
- Wong, J., Dinsmore, J., & Romani, R. 2023, in *AAS/High Energy Astrophysics Division*, Vol. 20, AAS/High Energy Astrophysics Division, 116.112
- Xie, F., Wong, J., La Monaca, F., et al. 2024, *ApJ*, 962, 92, doi: [10.3847/1538-4357/ad17ba](https://doi.org/10.3847/1538-4357/ad17ba)